

Cite this: *Chem. Sci.*, 2026, **17**, 3141

All publication charges for this article have been paid for by the Royal Society of Chemistry

Received 23rd July 2025
Accepted 7th December 2025

DOI: 10.1039/d5sc05521k
rsc.li/chemical-science

Introduction

Enzymes are attractive alternatives^{1–4} to synthetic small-molecule catalysts which frequently employ organic solvents, elevated temperatures, and precious metals, and thus compromise industrial and governmental sustainability goals.^{5,6} Despite the benefits of enzyme-catalyzed transformations, many valuable enzymes are yet to be translated into industrial settings due to the high costs arising from lack of enzyme reusability and a requirement for specific storage and/or reaction conditions. Silicatein, a naturally derived enzyme capable of catalyzing Si–O bond hydrolyses and condensations, is an established biotechnological target. Specifically, silicatein facilitates the synthesis of organosiloxanes^{7,8} and crystalline metal oxides^{9,10} – materials with extensive applications in cosmetics, optics and catalysis.¹¹ Application of silicatein in chemical synthesis is, however, yet to be realized due to its propensity to aggregate and precipitate from solution.^{7,11} To date, a variety of biochemical approaches have been investigated to improve the solubility of silicatein, with the most effective approach being the formation of a fusion protein of trigger factor (TF) and silicatein (TF-Sil α).^{7,12–14} However, despite

inclusion of the solubility tag, TF-Sil α is still prone to oligomerization.¹⁵ Accordingly, the availability of a silicatein preparation that is robust and generically applicable remains unmet.

Biomimetic crystallization is emerging^{16–18} as a promising materials approach to protein stabilization, with reports detailing the enhanced thermal, chemical and biological stability of enzymes following encapsulation and the potential for enzyme reuse following multiple catalytic cycles.^{19–21} Here, we report the production and characterization of two TF-Sil α @MOF composites derived from a zeolitic imidazole framework, ZIF-8, and a dicarboxylate-based MOF, Zn-BDC-NH₂ (Fig. 1). These Zn-based MOFs were selected for enzyme immobilization due to their established biocompatibility and

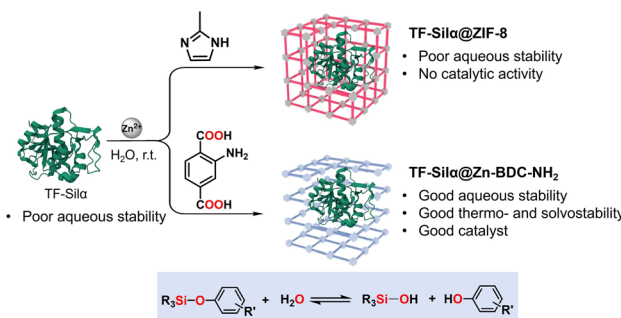


Fig. 1 Schematic of biomimetic crystallization of TF-Sil α in ZIF-8 (top, red) and Zn-BDC-NH₂ (bottom, blue). Catalytic activity of encapsulated enzyme shown in blue box.

^aDepartment of Chemistry, The University of Manchester, Oxford Road, Manchester, M13 9PL, UK. E-mail: imogen.riddell@manchester.ac.uk

^bManchester Institute of Biotechnology, University of Manchester, 131 Princess Street, Manchester, M1 7DN, UK. E-mail: L.S.Wong@manchester.ac.uk

^cDepartment of Physics, University of Warwick, Gibbet Hill Road, Coventry, CV4 7AL, UK



lack of toxicity,^{22,23} factors which minimize the risk of protein denaturation and will enable translation of these materials into sustainable chemical synthesis²⁴ and therapeutic settings.^{23,25} Whilst **TF-Sil α @ZIF-8** shows negligible catalytic performance, **TF-Sil α @Zn-BDC-NH₂** demonstrates comparable catalytic performance to the native **TF-Sil α** , in addition to benefitting from enhanced enzyme stability, ease of recycling and reduced long-term storage requirements.

Here, we demonstrate that proteins with unmet solubility and stability challenges can be encapsulated within MOFs and the protective framework enables reuse of the enzyme as well as elongation of its half-life at room temperature by 4.4-fold.

Results and discussion

Biomimetic crystallization of **TF-Sil α**

Initial experiments set out to evaluate MOF formation with **TF-Sil α** in the presence of zinc(II) nitrate and two separate organic linkers, 2-aminoterephthalic acid and 2-methylimidazole,^{16,20,26} with the aim of producing **TF-Sil α @Zn-BDC-NH₂** and **TF-Sil α @ZIF-8**, respectively. These ligands were chosen as they had been previously reported to be capable of generating framework materials with tunable properties including particle size, protein loading and hydrophobicity, each of which affects the encapsulated protein's catalytic performance.²⁷ Following established protocols,^{16,20,26} we combined solutions of zinc(II) nitrate, the appropriate organic linker and freshly isolated **TF-Sil α** (SI Section S3). The isolated precipitates were washed with water and methanol and then analyzed to determine their crystal structure, particle size, morphology, and to confirm the presence of **Sil α** .

Enzyme encapsulation in **Zn-BDC-NH₂**

Firstly, the encapsulation efficiency (EE, percentage of encapsulated protein) and loading content (LC, weight-percentage of protein in MOF) were calculated by quantifying the residual protein in the supernatant. In **TF-Sil α @Zn-BDC-NH₂** high EE values were achieved (96%), with LC values of approximately 10% (Table S3), which compares favorably with EE and LC values reported for other enzyme@MOF composites reported in the literature.^{16,19,20}

The **Zn-BDC-NH₂** biocomposite was then characterized using vibrational spectroscopy (FTIR), thermogravimetric analysis (TGA) and energy dispersive X-ray (EDX) spectroscopy. The FTIR spectrum for **TF-Sil α @Zn-BDC-NH₂** included a peak between 1600 and 1690 cm⁻¹ (Fig. S14a) that would be consistent with the amide I band from the protein.²⁸ However, the carboxylate stretch in the parent **Zn-BDC-NH₂** MOF also appeared in this region of the spectrum and thus could not confirm the incorporation of **TF-Sil α** . Closer inspection of the second-derivative FTIR spectrum (Fig. S15a and c) revealed that **TF-Sil α @Zn-BDC-NH₂** retained peaks attributed to α -helical peptide sequences (1659, 1652, and 1645 cm⁻¹),²⁹ these peaks were absent in the pristine MOF providing further evidence of protein encapsulation (Fig. S15a and c). As evidenced by the second-derivative FTIR spectrum, the characteristic secondary

structures of **TF-Sil α** including α -helices and β -sheets were preserved,²⁹ indicating the protein retained its conformation upon immobilization. This result was supported by CD spectroscopy experiments (Fig. S16a) which evaluated potential changes in the protein structure during the MOF nucleation process.³⁰ CD spectra recorded for **TF-Sil α** in the presence and absence of the BDC-NH₂ ligand were comparable (Fig. S16a), with both spectra clearly displaying α -helical features.

TGA of **TF-Sil α @Zn-BDC-NH₂** revealed a three-step weight decrease (Fig. S17). By comparison to previous reports of protein@MOF TGAs,^{31,32} the initial mass loss at lower temperatures ($T < 200$ °C) was attributed to water evaporation from the framework, followed by loss of the protein between 200 and 400 °C, with mass loss above 400 °C being attributed to MOF decomposition.³³ For **TF-Sil α @Zn-BDC-NH₂** a 20% weight loss was found from 300 to 400 °C, whilst only 12% mass reduction was observed for the parent **Zn-BDC-NH₂** in the absence of protein, which was attributed to BDC-NH₂ linker decomposition (SI Fig. S17c and d). Thus, this difference in the mass loss (i.e. 8%) could be assigned to the loss of **TF-Sil α** . However, as the protein loading and residual solvent content in the biocomposite vary amongst batches (Table S3), TGA only offers an estimation of the enzyme@MOF composition. Additionally, the EDX spectra for the **TF-Sil α @Zn-BDC-NH₂** particles clearly indicated signals corresponding to sulfur (Fig. S18), which must originate from cysteine residues within the **TF-Sil α** .

To determine protein localization within the MOF particles, a fusion protein comprised of **TF-Sil α** and enhanced green fluorescence protein (**TF-Sil α -eGFP**) was produced and encapsulated within the MOF. The **TF-Sil α -eGFP@Zn-BDC-NH₂** was assembled using analogous procedures to those previously employed, and no significant differences in the PXRD patterns (Fig. S31b) were recorded (see discussion below; Fig. S31) indicating no changes to the MOF structure following introduction of the eGFP domain. The biocomposite was then imaged by confocal laser scanning microscopy (CLSM) and co-localization of the MOF particles and green fluorescence was observed (Fig. 2). Subsequent optical sectioning of the MOF

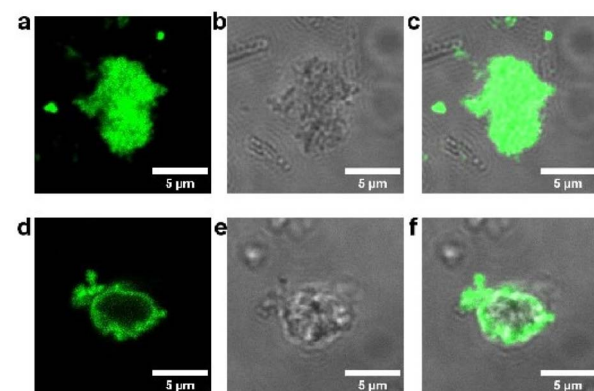


Fig. 2 Confocal laser scanning micrograph of **TF-Sil α -eGFP@Zn-BDC-NH₂**; (a) dark field excited at 488 nm, (b) bright field, and (c) merged. Confocal laser scanning micrograph of **TF-Sil α -eGFP** on **Zn-BDC-NH₂**; (d) dark field excited at 488 nm, (e) bright field and (f) merged.



particles showed that the fluorescence corresponding to the eGFP domain was present uniformly throughout all sections (Fig. S20 and S23), which is consistent with protein impregnation within the MOF structure. In contrast, control experiments in which **TF-Sil α -eGFP** was mixed with preformed **Zn-BDC-NH₂** particles resulted in the formation of aggregates with non-fluorescent cores indicative of protein binding exclusively on the surface of the MOF (Fig. 2, S24).

Topology and morphology of **TF-Sil α @Zn-BDC-NH₂**

The materials precipitated following biomimetic crystallization were also characterized using single-crystal electron diffraction (3D ED), PXRD, DLS and SEM. Three single crystals of **TF-Sil α @Zn-BDC-NH₂** were selected under cryogenic conditions for electron diffraction analysis (SI S4.5). Solution and refinement of the data supported formation of a previously reported 2D layered MOF structure.²⁶ In this MOF, each zinc(II) ion is bound to three BDC-NH₂ linkers and two water molecules, with the water protons directed out into the interlayer space (Fig. S25). The PXRD pattern (Fig. 3a) of the bulk material was consistent with the single-crystal data and no features corresponding to the protein were observed in either the 3D ED or PXRD data sets, which is consistent with a disordered arrangement of **TF-Sil α** within the crystalline MOF. Moreover, the **TF-Sil α @Zn-BDC-NH₂** diffraction patterns appeared identical to those of the parent structure lacking protein, **Zn-BDC-NH₂**, implying that enzyme incorporation did not influence the long-range order of this MOF (Table S6).

The crystal size and shape distributions were also studied by DLS and SEM. DLS data showed two distinct populations of **TF-Sil α @Zn-BDC-NH₂** crystals centered at hydrodynamic diameters (D_h) of 172 nm and 1.0 μ m (Fig. S33). SEM images of **TF-Sil α @Zn-BDC-NH₂** (Fig. 3b) displayed plate-shaped crystals with average diameters of around 1–3 μ m, alongside some smaller nanoparticles, consistent with the DLS results.

Synthesis and characterisation of **TF-Sil α @ZIF-8**

As a comparison, **TF-Sil α @ZIF-8** was also prepared since **ZIF-8** is one of the most studied MOFs for biomimetic crystallization.

This biocomposite also shows relatively high EE (86%) and LC (14%) values compared to reported enzyme@MOF systems.^{16,19,20} In FTIR spectra, an amide I band²⁸ was found at 1670 cm^{-1} which is absent in the spectrum of the enzyme-free ZIF, indicating **TF-Sil α** incorporation. Second derivative analysis of the FTIR spectrum indicates a redshift (4–7 cm^{-1}) of α -helical peaks, consistent with protein-MOF interactions,³⁴ but overall the peaks corresponding to secondary structure are preserved, supporting retention of the protein structure upon **ZIF-8** encapsulation (Fig. S15b and d). This result is consistent with CD experiments which indicate retention of α -helical features during mixing of **TF-Sil α** with 2-methylimidazole, as occurs during MOF nucleation³⁰ (Fig. S16b). TGA suggests no significant mass loss for pure **ZIF-8** between 200 and 350 $^\circ\text{C}$. In contrast, a 9.5% weight loss was observed across this temperature range for **TF-Sil α @ZIF-8**, corresponding to protein degradation. The EDX spectrum of the MOF particles also exhibited a sulfur signal that further confirmed enzyme incorporation. As with the **TF-Sil α @Zn-BDC-NH₂** composite, confocal micrographs of **TF-Sil α -eGFP@ZIF-8** indicated uniform fluorescence throughout all optical sections (Fig. S19 and S20), supporting the protein encapsulation within the MOF rather than adsorption on to its surface.

The topology and morphology of **TF-Sil α @ZIF-8** were also investigated. The PXRD pattern showed a primary topology of sodalite³⁵ (78.5%) with the peak at 11 degrees 2θ (Fig. S27 and S28) indicating a minor component of **ZIF-CO₃-1** (21.5%) within the mixture.³⁶ In contrast, the attempted synthesis of **ZIF-8** in the absence of **TF-Sil α** , but under otherwise identical conditions, occurred over a longer timeframe, gave lower isolated yields, and the PXRD patterns indicated the exclusive formation of **ZIF-L** (ref. 37 and 38) (Fig. S26). SEM revealed leaf-like particles of this material which also corresponds to the characteristic morphology of **ZIF-L**³⁷ (Fig. S36). This result is consistent with previous reports where the **ZIF-8** sodalite topology is favored over other crystalline forms when proteins that promote biomimetic crystallization are present.³⁹ The particle size distribution was further investigated with DLS. In contrast to **TF-Sil α @Zn-BDC-NH₂**, **TF-Sil α @ZIF-8** exhibited a large size polydispersity, with hydrodynamic diameters (D_h)

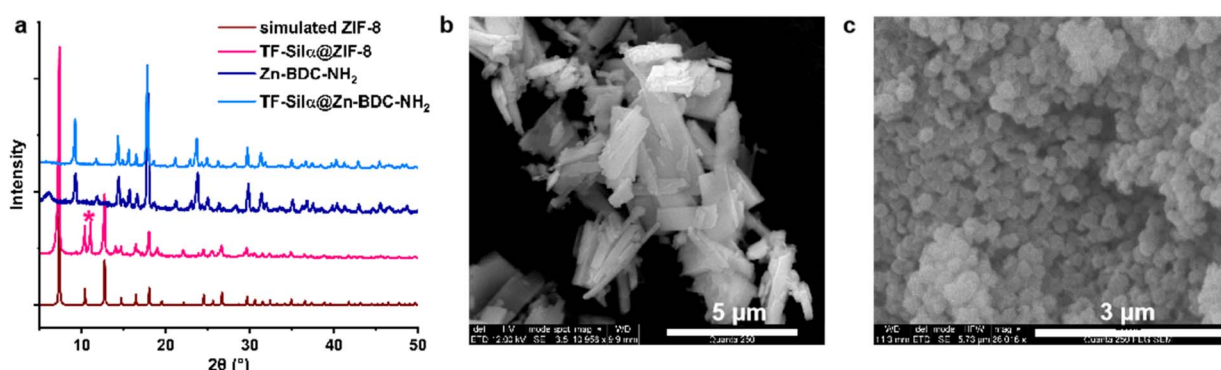


Fig. 3 Topology and morphology study. (a) PXRD patterns of simulated ZIF-8 (from ref. 35), TF-Sil α @ZIF-8, synthesized Zn-BDC-NH₂ and TF-Sil α @Zn-BDC-NH₂. The PXRD pattern for TF-Sil α @ZIF-8 is consistent with primarily a sodalite structure with small amount (21.5%) of ZIF-CO₃-1 mixture (marked with asterisk*). The PXRD patterns for Zn-BDC-NH₂, both in the presence and absence of TF-Sil α , correspond with a known 2D layered MOF structure (ref. 26). SEM images of (b) TF-Sil α @Zn-BDC-NH₂ plates and (c) three-dimensional TF-Sil α @ZIF-8 crystals.



ranging from 200 nm to 20 μm (Fig. S33). SEM images of **TF-Sil α @ZIF-8** revealed three-dimensional particles, similar to the rhombic dodecahedron morphology as previously reported,⁴⁰ and particle sizes were observed around 200 nm (Fig. 3c and S35). This difference in the apparent sizes from the two analyses was attributed to particle aggregation due to the hydrophobic nature of **ZIF-8**.²⁷

Catalytic performance of encapsulated **TF-Sil α**

To quantify the enzymatic activity of the immobilized **TF-Sil α** with regard to Si–O bond hydrolysis, a colorimetric assay involving the hydrolysis of the chromogenic substrate tert-butyldimethyl(2-methyl-4-nitrophenoxy)silane (TBDMS-OMeNp)⁴¹ was performed (Fig. 4a). Here, hydrolysis of the scissile bond results in the release of a highly absorbing nitrophenolate that can be quantified by UV-Vis spectrophotometry. In these assays, the **TF-Sil α @Zn-BDC-NH₂** particles maintained an apparently stable colloid for over 20 hours (Fig. S38) and the hydrolytic activity could be measured with a high degree of reproducibility (Fig. 4b and S40). In contrast, in analogous experiments the **TF-Sil α @ZIF-8** particles precipitated rapidly resulting in large measurement errors (Fig. S38). The recorded hydrolytic activity was, however, consistent with background hydrolysis from the MOF and did not support any enzymatic activity (Fig. S39).

Since the overall reaction rate is dependent on both substrate diffusion within the matrix and the enzyme activity,

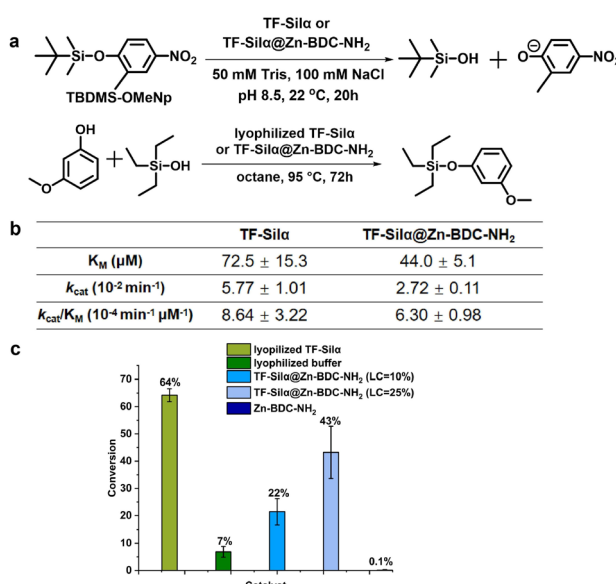


Fig. 4 Catalytic performance of free and encapsulated **TF-Sil α** . (a) Schemes representing the hydrolysis (top) and condensation reactions (bottom). (b) Apparent kinetic parameters of free (ref. 30) and encapsulated **TF-Sil α** catalyzing the hydrolysis of TBDMS-OMeNp. Results are averaged from 3 measurements (c) Percentage conversions of 3-methoxyphenol to triethyl(3-methoxyphenoxy)silane. The reaction was catalyzed by lyophilized or encapsulated **TF-Sil α** (loading content 10% or 25%) and their negative controls (lyophilized buffer and pure MOFs). The total **TF-Sil α** concentration in the lyophilised and encapsulated **TF-Sil α** preparations was kept constant at 67 μM in the reaction mixtures.

the effectiveness factor was calculated to identify any differences between the mass transfer in **TF-Sil α @Zn-BDC-NH₂** and the free enzyme.^{42,43} It was found that there was no significant change in effectiveness factor (Table S7) when increasing the substrate concentration from 20 μM to 60 μM , suggesting that mass transfer limitations are insignificant. The Michaelis–Menten model of enzyme kinetics could therefore be applied to these enzyme@MOF systems.^{44,45} The apparent Michaelis–Menten kinetic parameters K_{M} , k_{cat} and $k_{\text{cat}}/K_{\text{M}}$ were determined and compared with parameters obtained for the free enzyme⁴¹ (Fig. 4b). It was found that the apparent k_{cat} for **TF-Sil α @Zn-BDC-NH₂** was similar but slightly slower than for the free **TF-Sil α** . The apparent substrate binding was, however, improved upon encapsulation as evidenced by lower K_{M} compared to free **TF-Sil α** . The reduced K_{M} value might indicate reduced conformational freedom of the enzyme upon encapsulation that enhances enzyme–substrate affinity.^{33,46}

Overall, **TF-Sil α @Zn-BDC-NH₂** displays comparable hydrolysis activity to free **TF-Sil α** as indicated by the similarity in the catalytic efficiency ($k_{\text{cat}}/K_{\text{M}}$) values. The observation that **TF-Sil α @Zn-BDC-NH₂** outperforms **TF-Sil α @ZIF-8** in catalysis is attributed to the 2D layered structure of the former, which facilitates substrate diffusion between the interlayer spaces and renders the encapsulated enzyme more accessible. This is consistent with previous reports which highlight substrate diffusion as a key challenge for three-dimensional MOF structures.^{47,48}

Next, the condensation activity of the immobilized enzyme was compared with the lyophilized **TF-Sil α** .⁴⁹ Here, a model reaction involving 3-methoxyphenol and triethylsilanol as substrates was investigated (Fig. 4a). The condensation product was quantified by GC-MS following 72 hours heating at 95 °C in octane. The thermal and chemical robustness of the **TF-Sil α @MOFs** enabled their direct use in the reaction. Both lyophilized and encapsulated enzyme gave higher conversions compared to the negative control groups consisting of either the additives used to prepare the lyophilized enzyme (phosphate buffer salts and 18-crown-6) or the MOF alone without enzyme (Fig. 4c). It was found that increasing protein loading (LC) from 10% to 25%, increased the reaction conversion by two-fold (22 to 43%) even at equivalent quantities of enzyme.

As a comparison, **TF-Sil α @ZIF-8** at 10% LC showed 26% conversion, similar to **TF-Sil α @Zn-BDC-NH₂**. However, control studies with **ZIF-8** alone gave a 6% conversion, attributed to general base catalysis by its 2-methyl imidazole linkers (Fig. S42). Overall, **TF-Sil α @Zn-BDC-NH₂** retained both hydrolysis and condensation activity and when the protein loading in the MOF was properly tuned **TF-Sil α @Zn-BDC-NH₂** retained \sim 70% of the activity observed for **TF-Sil α** in both reactions.

Stability and reusability of **TF-Sil α @Zn-BDC-NH₂**

As encapsulation has been shown to improve protein stability under conditions that are not ordinarily biocompatible^{16,27,46} **TF-Sil α @Zn-BDC-NH₂** was next evaluated to see if this material exhibited enhanced thermal and chemical stability. Here, the **TF-Sil α** free enzyme and **TF-Sil α @Zn-BDC-NH₂** were both



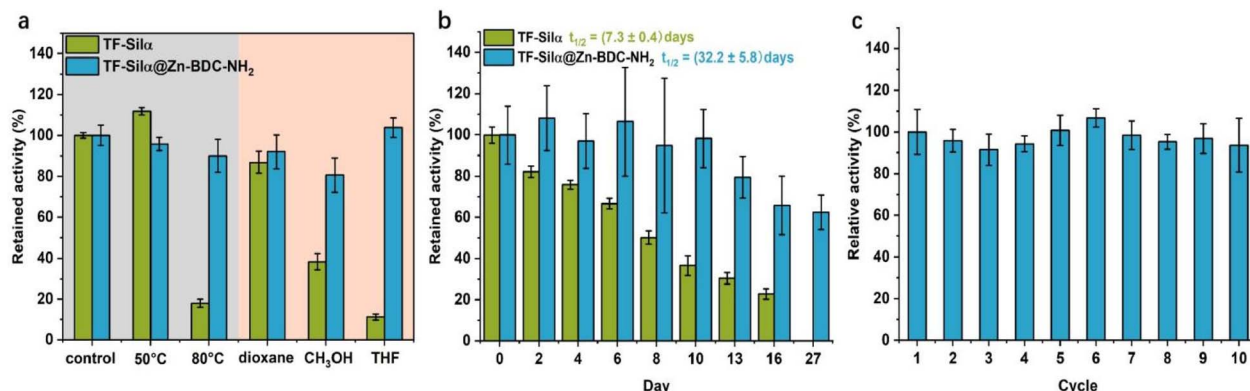


Fig. 5 Stability and reusability investigation. (a) Relative activity of TF-Sil α and TF-Sil α @Zn-BDC-NH₂ after exposure to elevated temperature or organic solvents for 2 h. (b) Retained activity of TF-Sil α and TF-Sil α @Zn-BDC-NH₂ as a function of time when stored in buffered solution at room temperature. The half-life of free and encapsulated enzyme at 20 °C is found to be 7.3 ± 0.4 days and 32.2 ± 5.8 days, respectively. The activity was calculated as the initial rate during first 100 minutes, and the non-treated control group was normalized to 100% activity. (c) Relative activity of recycled TF-Sil α @Zn-BDC-NH₂ over ten cycles; results are averaged from three measurements. Error bars represent standard error of mean.

exposed to elevated temperatures (50 °C and 80 °C) or the organic solvents dioxane, methanol and THF (as representative examples of non-polar and polar solvents) for 2 hours prior to measuring their hydrolytic activity (see S5.6). PXRD analysis following heat or solvent treatment confirmed no structural degradation of the MOF had taken place under any of the conditions.

In terms of thermotolerance, little difference in the hydrolytic activity between the encapsulated and free enzyme was observed at 50 °C. Enhanced stability was, however, clearly demonstrated for the encapsulated proteins that had been heat-treated at 80 °C for 2 h, whereby the free silicatein lost 80% of its hydrolytic activity relative to the untreated TF-Sil α control whilst the encapsulated enzyme exhibited only a minor reduction in activity (~10%, Fig. 5a).

Similarly, enhanced chemical stability was observed for TF-Sil α @Zn-BDC-NH₂ compared with the free enzyme, especially when treated with the polar solvents methanol and THF (Fig. 5a). Polar solvents are well documented to disrupt the secondary and tertiary structures of proteins resulting in loss of enzymatic activity.^{49–51} Here, confinement inside the MOF restricts protein unfolding, thus inhibiting loss of catalytic activity.

To investigate the longevity of biocatalytic activity, TF-Sil α and TF-Sil α @Zn-BDC-NH₂ were stored at room temperature for 16–27 days and their hydrolytic activity was monitored over time. Whilst a gradual decrease in hydrolytic activity was observed for the free enzyme over time, no significant loss of activity for the TF-Sil α @Zn-BDC-NH₂ was observed in the first 10 days followed subsequently by a gradual decline (Fig. 5b). Even so, the encapsulated enzyme retained ~70% of its original activity after 27 days, while the free enzyme showed no activity after this time. The half-lives ($t_{1/2}$) of TF-Sil α and TF-Sil α @Zn-BDC-NH₂ at 20 °C were determined to be to be (7.3 ± 0.4) days and (32.2 ± 5.8) days, respectively. This result suggests encapsulation elongates the TF-Sil α lifetime 4.4-fold and demonstrates the enhanced stability of TF-Sil α @Zn-BDC-NH₂ over the native protein.

In regard to the ease of recycling of the immobilized enzyme, the encapsulated enzyme particles were found to be readily separated by centrifugation post-reaction. These recovered enzyme@MOF particles were then subjected to nine further reaction cycles without any significant loss of activity (Fig. 5c). Since the free TF-Sil α cannot be separated from the reaction mixture, a comparative experiment was carried out whereby a solution of TF-Sil α was left to stand at 22 °C for different time periods. These time periods were chosen to correspond to the amount of time the enzyme would have been exposed to the enzyme@MOF reaction conditions (0–100 h) prior to hydrolysis, mimicking the reaction conditions during the catalyst recycling process. In this case, only 50–60% of the activity was retained relative to freshly defrosted isolated enzyme (Fig. S43). The ease of separation and the enhanced stability of the TF-Sil α @Zn-BDC-NH₂ both, therefore, contribute to its recyclability, enabling TF-Sil α @Zn-BDC-NH₂ to be reused under standard assay conditions for over 10 cycles without any obvious reduction of bioactivity. In contrast, in absence of the MOF each aliquot of enzyme must be freshly defrosted prior to use.

Conclusions

Encapsulation of the otherwise unstable protein TF-Sil α through biomimetic crystallization within the 2D layered MOF, Zn-BDC-NH₂, is shown to significantly improve its operational stability. Specifically in the case of TF-Sil α @Zn-BDC-NH₂, biocatalytic activity is retained in both the model silyl ether hydrolysis and formation reactions, showing that neither the self-assembly process nor the framework deactivates the protein. Furthermore, the encapsulated TF-Sil α shows enhanced thermo- and solvostability in comparison to the free enzyme. Additionally, excellent reusability was demonstrated over ten catalytic cycles with the half-life of TF-Sil α at room temperature extended 4.4-fold upon MOF immobilization. This increase in room temperature stability presents opportunities to improve the stability and practical handling of fragile proteins, circumventing the need for cold storage for periods as



long as a week. In contrast, despite being the most extensively studied biomimetic crystallization material, the **TF-Sil_{0.8}@ZIF-8** biocomposite suffered from poor colloidal stability which negatively impacted its catalytic performance.

Overall, biomimetic crystallization offers a promising approach to stabilize fragile enzymes for process intensification. Future work will look to diversify the range of MOFs suitable for encapsulation enabling application of this technology to other sectors including the development of non-toxic MOFs for use in delivery of therapeutic proteins.

Author contributions

Conceptualization, T. Z., L. S. W. and I. A. R.; methodology, T. Z.; Investigation, T. Z., X. W., J. D. W., G. F. S. W., J. P. T.; formal analysis, T. Z.; validation, T. Z., L. S. W. and I. A. R.; writing – original draft, T. Z.; writing – review & editing, T. Z., L. S. W. and I. A. R.; visualization, T. Z., I. A. R.; resources, supervision and funding acquisition, L. S. W. and I. A. R.

Conflicts of interest

There are no conflicts to declare.

Data availability

The data supporting this article have been included as part of the supplementary information (SI). Supplementary information: substrate and calibrant synthesis, enzyme and enzyme@-MOFs preparation, FTIR, CD, TGA, EDX, CLSM, 3D ED, PXRD, DLS, SEM and enzymatic activity study is available. See DOI: <https://doi.org/10.1039/d5sc05521k>.

Supplementary crystallographic data in the form of the CIF is available at CCDC 2418698: Experimental Crystal Structure Determination, 2025, DOI: [10.5517/ccdc.csd.cc2m5vj6](https://doi.org/10.5517/ccdc.csd.cc2m5vj6).⁵²

Acknowledgements

TZ acknowledges the BBSRC DTP (BB/T008725/1) for a studentship. XW acknowledges CSC for scholarship (202006170024). IAR acknowledges support through a Royal Society University Research Fellowship (URF\R1\180414) and an EPSRC New Investigators Award (EP/T017473/1). IAR also thanks the University of Manchester XRD Facility for access to diffractometers. LSW thanks the EPSRC for support under grant EP/S013539/1. The authors acknowledge Yangyang Feng and the Department of Materials for their support in collecting SEM images. The authors thank the NCS for granting rapid access to the National Electron Diffraction Facility under EPSRC funding (EP/X014606/1 & EP/X014444/1, A National Electron Diffraction Facility for Nanomaterial Structural Studies), as well as the University of Warwick X-ray Research Technology Platform for provision of further analysis facilities. The Gatan Elsa specimen holder was procured under EPSRC funding (EP/R019428/1).

Notes and references

- 1 S. Wu, R. Snajdrova, J. C. Moore, K. Baldenius and U. T. Bornscheuer, *Angew. Chem., Int. Ed.*, 2021, **60**, 88–119.
- 2 L. E. Zetzsche and A. R. H. Narayan, *Nat. Rev. Chem.*, 2020, **4**, 334–346.
- 3 K. Chen and F. H. Arnold, *Nat. Catal.*, 2020, **3**, 203–213.
- 4 M. Ohashi, C. S. Jamieson, Y. Cai, D. Tan, D. Kanayama, M.-C. Tang, S. M. Anthony, J. V. Chari, J. S. Barber, E. Picazo, T. B. Kakule, S. Cao, N. K. Garg, J. Zhou, K. N. Houk and Y. Tang, *Nature*, 2020, **586**, 64–69.
- 5 S. Paramanathan, C. Farrukh, R. Phaal and D. Probert, *R D Manag.*, 2004, **34**, 527–537.
- 6 F. Biermann, T. Hickmann, C.-A. Sénit, M. Beisheim, S. Bernstein, P. Chasen, L. Grob, R. E. Kim, L. J. Kotzé, M. Nilsson, A. Ordóñez Llanos, C. Okereke, P. Pradhan, R. Raven, Y. Sun, M. J. Vijge, D. van Vuuren and B. Wicke, *Nat. Sustain.*, 2022, **5**, 795–800.
- 7 S. Y. Tabatabaei Dakhili, S. A. Caslin, A. S. Faponle, P. Quayle, S. P. de Visser and L. S. Wong, *Proc. Natl Acad. Sci.*, 2017, **114**, E5285–E5291.
- 8 S. E. Wolf, U. Schlossmacher, A. Pietuch, B. Mathiasch, H.-C. Schröder, W. E. G. Müller and W. Tremel, *Dalton Trans.*, 2010, **39**, 9245–9249.
- 9 J. L. Sumerel, W. Yang, D. Kisailus, J. C. Weaver, J. H. Choi and D. E. Morse, *Chem. Mater.*, 2003, **15**, 4804–4809.
- 10 D. Kisailus, J. H. Choi, J. C. Weaver, W. Yang and D. E. Morse, *Adv. Mater.*, 2005, **17**, 314–318.
- 11 R. L. Brutcher and D. E. Morse, *Chem. Rev.*, 2008, **108**, 4915–4934.
- 12 K. Godigamuwa, K. Nakashima, J. Okamoto and S. Kawasaki, *Biomacromolecules*, 2020, **21**, 2922–2928.
- 13 H. Oguri, K. Nakashima, K. Godigamuwa, J. Okamoto, Y. Takeda, F. Okazaki, M. Sakono and S. Kawasaki, *J. Biosci. Bioeng.*, 2022, **133**, 222–228.
- 14 T. N. Vigil, M.-J. C. Rowson, A. J. Frost and B. W. Berger, *Mater. Adv.*, 2023, **4**, 662–668.
- 15 E. I. Sparkes, R. A. Kettles, C. S. Egedeuzu, N. L. Stephenson, S. A. Caslin, S. Y. Tabatabaei Dakhili and L. S. Wong, *Biomolecules*, 2020, **10**, 1209.
- 16 K. Liang, R. Ricco, C. M. Doherty, M. J. Styles, S. Bell, N. Kirby, S. Mudie, D. Haylock, A. J. Hill, C. J. Doonan and P. Falcaro, *Nat. Commun.*, 2015, **6**, 7240.
- 17 J. Liu, J. Liang, J. Xue and K. Liang, *Small*, 2021, **17**, 2100300.
- 18 J. C. Díaz and M. Giménez-Marqués, *Chem. Comm.*, 2024, **60**, 51–54.
- 19 I. Akpinar, X. Wang, K. Fahy, F. Sha, S. Yang, T.-w. Kwon, P. J. Das, T. Islamoglu, O. K. Farha and J. F. Stoddart, *J. Am. Chem. Soc.*, 2024, **146**, 5108–5117.
- 20 D. Jordahl, Z. Armstrong, Q. Li, R. Gao, W. Liu, K. Johnson, W. Brown, A. Scheiwiller, L. Feng, A. Ugrinov, H. Mao, B. Chen, M. Quadir, H. Li, Y. Pan and Z. Yang, *ACS Appl. Mater. Interfaces*, 2022, **14**, 51619–51629.
- 21 F. C. Herbert, S. S. Abeyrathna, N. S. Abeyrathna, Y. H. Wijesundara, O. R. Brohlin, F. Carraro, H. Amenitsch, P. Falcaro, M. A. Luzuriaga, A. Durand-Silva,

S. D. Diwakara, R. A. Smaldone, G. Meloni and J. J. Gassensmith, *Nat. Comm.*, 2021, **12**, 2202.

22 S. Kumari, T. S. Howlett, R. N. Ehrman, S. Koirala, O. Trashi, I. Trashi, Y. H. Wijesundara and J. J. Gassensmith, *Chem. Sci.*, 2023, **14**, 5774–5782.

23 Y. T. Dang, M.-H. D. Dang, N. X. D. Mai, L. H. T. Nguyen, T. B. Phan, H. V. Le, T. L. H. Doan and J. Sci, *Adv. Mater. Dev.*, 2020, **5**, 560–565.

24 H. R. Kalhor, Z. Piraman and Y. Fathali, *iScience*, 2023, **26**, 107807.

25 Q. Wang, Y. Sun, S. Li, P. Zhang and Q. Yao, *RSC Adv.*, 2020, **10**, 37600–37620.

26 X. Wang, S. P. Singh, T. Zhang, R. Andrews, M. G. Lizio, G. F. S. Whitehead and I. A. Riddell, *Inorg. Chem.*, 2024, **63**, 9801–9808.

27 W. Liang, H. Xu, F. Carraro, N. K. Maddigan, Q. Li, S. G. Bell, D. M. Huang, A. Tarzia, M. B. Solomon, H. Amenitsch, L. Vaccari, C. J. Sumby, P. Falcaro and C. J. Doonan, *J. Am. Chem. Soc.*, 2019, **141**, 2348–2355.

28 J. Kong and S. Yu, *Acta Biochim. Biophys. Sin.*, 2007, **39**, 549–559.

29 A. Barth, *BBA - Bioenergetics*, 2007, **1767**, 1073–1101.

30 B. P. Carpenter, B. Rose, E. M. Olivas, M. X. Navarro, A. R. Talosig, P. J. Hurst, G. Di Palma, L. Xing, R. Guha, S. M. Copp and J. P. Patterson, *J. Mater. Chem. A*, 2024, **12**, 813–823.

31 C. Wang, G. Sudlow, Z. Wang, S. Cao, Q. Jiang, A. Neiner, J. J. Morrissey, E. D. Kharasch, S. Achilefu and S. Singamaneni, *Adv. Healthc. Mater.*, 2018, **7**, 1800950.

32 X. Wu, J. Ge, C. Yang, M. Hou and Z. Liu, *Chem. Comm.*, 2015, **51**, 13408–13411.

33 F. Lyu, Y. Zhang, R. N. Zare, J. Ge and Z. Liu, *Nano Lett.*, 2014, **14**, 5761–5765.

34 D. Tocco, D. Chelazzi, R. Mastrangelo, A. Casini, A. Salis, E. Fratini and P. Baglioni, *J. Colloid Interface Sci.*, 2023, **641**, 685–694.

35 X.-C. Huang, Y.-Y. Lin, J.-P. Zhang and X.-M. Chen, *Angew. Chem., Int. Ed.*, 2006, **45**, 1557–1559.

36 F. Carraro, M. d. J. Velásquez-Hernández, E. Astria, W. Liang, L. Twilight, C. Parise, M. Ge, Z. Huang, R. Ricco, X. Zou, L. Villanova, C. O. Kappe, C. Doonan and P. Falcaro, *Chem. Sci.*, 2020, **11**, 3397–3404.

37 A. Deacon, L. Briquet, M. Malankowska, F. Massingberd-Mundy, S. Rudić, T. I. Hyde, H. Cavaye, J. Coronas, S. Poulston and T. Johnson, *Commun. Chem.*, 2022, **5**, 1–10.

38 R. Chen, J. Yao, Q. Gu, S. Smeets, C. Baerlocher, H. Gu, D. Zhu, W. Morris, O. M. Yaghi and H. Wang, *Chem. Commun.*, 2013, **49**, 9500–9502.

39 H. Wang, L. Han, D. Zheng, M. Yang, Y. H. Andaloussi, P. Cheng, Z. Zhang, S. Ma, M. J. Zaworotko, Y. Feng and Y. Chen, *Angew. Chem., Int. Ed.*, 2020, **59**, 6263–6267.

40 O. M. Linder-Patton, T. J. De Prinse, S. Furukawa, S. G. Bell, K. Sumida, C. J. Doonan and C. J. Sumby, *CrystEngComm*, 2018, **20**, 4926–4934.

41 Y. Lu, C. S. Egedeuzu, P. G. Taylor and L. S. Wong, *Biomolecules*, 2024, **14**, 492.

42 A. B. Muley, K. H. Mulchandani and R. S. Singhal, in *Methods in Enzymology*, ed. C. V. Kumar, Academic Press, 2020, vol. 630, pp. 39–79.

43 A. B. Muley, A. S. Thorat, R. S. Singhal and K. Harinath Babu, *Int. J. Biol. Macromol.*, 2018, **118**, 1781–1795.

44 J. Liang, M. Y. Bin Zulkifli, J. Yong, Z. Du, Z. Ao, A. Rawal, J. A. Scott, J. R. Harmer, J. Wang and K. Liang, *J. Am. Chem. Soc.*, 2022, **144**, 17865–17875.

45 R. Greifenstein, T. Ballweg, T. Hashem, E. Gottwald, D. Achauer, F. Kirschhöfer, M. Nusser, G. Brenner-Weiß, E. Sedghamiz, W. Wenzel, E. Mittmann, K. S. Rabe, C. M. Niemeyer, M. Franzreb and C. Wöll, *Angew. Chem., Int. Ed.*, 2022, **61**, e202117144.

46 Y.-M. Li, J. Yuan, H. Ren, C.-Y. Ji, Y. Tao, Y. Wu, L.-Y. Chou, Y.-B. Zhang and L. Cheng, *J. Am. Chem. Soc.*, 2021, **143**, 15378–15390.

47 G. Chen, S. Huang, X. Kou, F. Zhu and G. Ouyang, *Angew. Chem., Int. Ed.*, 2020, **59**, 13947–13954.

48 Y. Tu, H. Li, T. Tu and Q. Zhang, *CCS Chem.*, 2021, **4**, 872–879.

49 E. I. Sparkes, C. S. Egedeuzu, B. Lias, R. Sung, S. A. Caslin, S. Y. Tabatabaei Dakhili, P. G. Taylor, P. Quayle and L. S. Wong, *Catalysts*, 2021, **11**, 879.

50 S. Hwang, Q. Shao, H. Williams, C. Hilty and Y. Q. Gao, *J. Phys. Chem. B*, 2011, **115**, 6653–6660.

51 Y. Yu, J. Wang, Q. Shao, J. Shi and W. Zhu, *Sci. Rep.*, 2016, **6**, 19500.

52 CCDC 2418698, Experimental Crystal Structure Determination, 2025, DOI: [10.5517/ccdc.csd.cc2m5vj6](https://doi.org/10.5517/ccdc.csd.cc2m5vj6).

